Pollution 2022, 8(3): 779-791
DOI: 10.22059/POLL.2022.331685.1202

RESEARCH PAPER

Preparation and Photocatalytic application of Ternary Fe_3O_4/GQD/g-C_3N_4 Heterostructure Photocatalyst for RhB Degradation

Hourieh Mirzaei[1], Mohammad Hossein Ehsani[1], Alireza Shakeri[2], Mohammad Reza Ganjali[2] and Alireza Badiei[2*]

[1] Department of Physics, Semnan University, P. O. Box 35131-19111, Semnan, Iran
[2] School of Chemistry, College of Science, University of Tehran, P. O. Box 14155-6455 Tehran, Iran

Received: 03.10.2021, Revised: 18.02.2022, Accepted: 25.02.2022

Abstract
Preparation of an efficient hybrid structure photocatalyst for photocatalytic decomposition has been considered a great option to develop renewable technologies for environmental remediation. Herein, ternary magnetic Fe_3O_4/GQD/g-C_3N_4 nanocomposite (FGC) was prepared using the ball mill method. Binary nanocomposites Fe_3O_4/g-C_3N_4 (F/CN) and GQD/g-C_3N_4 (G/CN) were prepared to compare photocatalytic activity with FGC. The performance of photocatalysts for degradation of rhodamine B (RhB) was studied. EDX results showed that Fe_3O_4, GQD and g-C_3N_4 nanoparticles (NPs) are uniformly distributed in the FGC. The FGC nanocomposite shows superparamagnetic behaviour with a saturation magnetization of 12 emu/g, which makes it favourable compound for magnetic separation procedure. Photocatalytic activity of FGC (100%) was much higher than those of the G/CN (88%) and F/CN (77%) photocatalysts. The superior activity of FGC compared to binary composites was attributed to broader absorption in the visible light band and greater suppression of electron-hole recombination. The photocatalytic degradation of RhB using FGC was consistent with pseudo-first-order kinetics. The reusability of FGC was examined for four runs and no noticeable decrease was observed with the same irradiation time for each run. Finally, it can be argued that FGC photocatalyst can be an efficient semiconductor for the degradation of organic dyes from wastewater.

Keywords: Graphene quantum dots, G-C_3N_4, RhB, Visible-light, Nanocomposites

INTRODUCTION

Today, the issue of water pollution becomes a severe problem for our humans (Dalrymple et al. 2010; Alsaleh & Abdul-Rahim 2021). Recently, semiconductor-based photocatalysis strategy has been used as one of the advanced oxidation processes (AOPs) that uses semiconductors and sunlight to eliminate organic pollutants (Esplugas et al. 2002; Giannakis et al. 2017; Karami et al. 2020). In this process, the pollutant molecules are oxidized over a catalyst under ultraviolet (UV) or visible light irradiation (Palmisano et al. 2007). The basis of the successful performance of photocatalysis is selection of an appropriate semiconductor photocatalyst. Since the advent of the photocatalysis technology, various materials have been developed as photocatalysts (Ghanbari & Salavati-Niasari 2018; Yahya et al. 2018). The first researches were mainly focused on metal oxide semiconductors, but during the years, many efforts have been made to make metal-free semiconductors. In 2009, polymer graphitic carbon nitride (g-C_3N_4), that is composed of two earth-abundant elements, was introduced as an attractive photocatalytic semiconductor (Azimi et al. 2018b; Sudhaik et al. 2018; Akhundi et al. 2020). However, the high recombination rate of the photogenerated electron-hole pairs and the low specific area

* Corresponding author Email: abadiei@khayam.ut.ac.ir

of pure g-C_3N_4 limited its photocatalytic performance. Several strategies can be employed to improve photocatalytic performance of g-C_3N_4 including doping with metal or non-metal elements, increasing of the surface-to-volume ratio and modifying with other semiconductors. Especially, significant progress has been attained in the coupling of g-C_3N_4 with carbonaceous materials such as carbon dots, graphene quantum dots, carbon nanotubes and fullerene (Zhang et al. 2012; Barvin et al. 2019). Carbon materials have unique properties such as good electronic conductivity and high electron reservoir ability, allowing increased charge separation. Among various kinds of this materials, GQD has high specific surface area which provides abundant active sites for photocatalytic reaction (Hong et al. 2016). For example, Hong et al. prepared metal-free CQD/g-C_3N_4 heterostructure photocatalyst through a simple low-temperature process in which the surface of g-C_3N_4 nanosheets was anchored by CQDs (Hong et al. 2016). CQD/g-C_3N_4 were shown an increased the photocatalytic performance toward RhB and tetracycline hydrochloride degradation. In another study, g-C_3N_4/GO aerogel heterojunctions were fabricated by a hydrothermal process which was coupled with self-assembly method. G-C_3N_4/GO exhibits high photocatalytic activity for photodegradation of methyl orange (92%) under visible light irradiation for 4 h. In another research, g-C_3N_4/RGO was thermally prepared, showed excellent photocatalytic activity for RhB degradation (98.3%) after 80 min. Despite the many benefits of g-C_3N_4, its separation remains a major concern. Many effective techniques have been used for the separation of photocatalytic materials. Magnetic separation, in contrast with other methods like filtration and centrifugation, has many unique advantages such as ease of use, cost-effectiveness and quick separation (Dai et al. 2014; Tong et al. 2015; Azimi et al. 2018). Thus, the recovery problem of g-C_3N_4 particles can be solved by coupling of g-$C_3N_4$with the magnetic species. Recently, Mousavi and et. al introduced the g-C_3N_4/Fe_3O_4/Ag_3PO_4/Co_3O_4 heterogeneous quaternary composite to photocatalytic degradation of RhB under visible light irradiation. The results proved that calcination of the sample for 2h at 300 °C showed maximum photocatalytic effectiveness compared to other samples (Mousavi & Habibi-Yangjeh 2017). In another study, Ag_2O/g-C_3N_4 /Fe_3O_4 was synthesized as a ternary composite and tested its photocatalytic activity. The results showed that as-prepared photocatalyst degraded RhB (98.3%) after 60 min under visible light (Akhundi & Habibi-Yangjeh 2016).

In the present study, we successfully prepared ternary (FGC) and binary systems (F/CN and G/CN) nanocomposites for photocatalytic RhB degradation under visible-light irradiation. The solar-driven RhB photocatalytic degradation for ternary composite (FGC) was much better than that of the binary composites. The ternary composite could be easily collected and recycled using a suitable magnetic field. Also, the four successive recycling tests showed the high photocatalytic stability of the catalyst, with simple recovery operation owing to its magnetic property.

MATERIAL AND METHODS

Iron (II) chloride ($FeCl_2$. $4H_2O$), iron (III) chloride ($FeCl_3$. $6H_2O$), ammonia (NH_4OH), hydrochloric acid (HCl) and sodium hydroxide (NaOH) were purchased from Sigma-Aldrich and used without further purification. Melamine ($C_3H_6N_6$) and methanol were bought from Merck and used without further purification. The citric acid ($C_6H_8O_7$) was supplied by TRIVENI CHEMICALS LIMITED and used without further purification.

Nanosized magnetite was prepared by controlled chemical co-precipitation of Fe^{2+} and Fe^{3+} (1:2 ratio) from ammoniacal medium at 80° C under nitrogen atmosphere. In a typical experiment, 0.02 mol of ferrous sulphate and 0.04 mol of $FeCl_3$ were dissolved in 200 ml of de-ionized and de-oxygenated water. The resulting solution was vigorously stirred and heated to 80° C under nitrogen atmosphere. Subsequently, about 12 ml of 25% ammonia solution was injected into the flask and stirring was continued for another 20 minutes to allow the growth of the nanoparticles. The solution was then cooled to room temperature and the resulting particles

were centrifuged followed by repeated washing with distilled water. The pH of the suspension was brought to neutral by the addition of dilute HCl, and the particles were rewashed with distilled water (Akhundi & Habibi-Yangjeh 2016).

Pyrolysis method is used to prepared graphene quantum dots (GQDs). 2 g of citric acid was heated and melted, which then turned dark orange in 25-30 minutes (Hong et al. 2016).

For synthesizing g-C_3N_4, 5 g of melamine were placed into a 50 mL covered alumina crucible, then calcined from 25 °C to 550 °C with a heating rate of 2.3 °C/min. With further thermal polymerization reaction for 4 h at 550 °C, the g-C_3N_4 powders were obtained through grinding after cooling to the room temperature (Rehman et al. 2019).

To prepare the Fe_3O_4/g-C_3N_4 nanocomposite, 100 mg g-C_3N_4 were dispersed in 50 ml of DI water by ultrasound for 30 min. Meanwhile, 1 mg of Fe_3O_4 nano particles was added into 10 mL of DI water by ultrasound for 15 min. Then, we added the suspension of Fe_3O_4 nano particles to the suspension of g-C_3N_4 drop by drop under vigorous stirring. After that, the obtained mixed suspension was sealed and stirred for 24 h. Finally, the product was dried at 60 °C for 24 h in a vacuum drying oven and then annealed at 150 °C in the vacuum drying oven for 2 h (Liu et al. 2014).

To prepare the GQD/g-C_3N_4 nanocomposite, 0.3 g of as-prepared pure g-C_3N_4 was added into 50 mL of methanol, then ultrasonically dispersed for 30 min. Subsequently, the GQD dispersion liquid was added into the g-C_3N_4 /methanol mixture, and continuously stirred at 40 °C until the methanol and water were completely removed (Hong et al. 2016).

For the synthesis of FGC nanocomposite, firstly, the Fe_3O_4 powder was prepared by co-precipitation method (Safee et al. 2010). The G/CN Binary nanocomposite was prepared according to the previously reported literatures (Zheng et al. 2012; Naik et al. 2017; Wang et al. 2017). Finally, for FGC preparation, 0.1 g of Fe_3O_4 powder and 0.5 g of G/CN powder were ball milled with a pellet for 1 h. Then, the obtained powder was dispersed into 40 mL of DI water by ultrasonic irradiation for 2 h. The product was centrifuged and dried in an oven at 70 ° C for 4 h (Fig. 1).

Field emission scanning electron microscopy (FESEM) images were obtained by Tescan-Mira3 equipment. Powder X-ray diffraction (XRD) by using a Bruker D5000 diffractometer with Cu Ka radiation (λ=0.15418 nm) was operated to study the phase structures of the samples. N_2 adsorption–desorption isotherm was performed with a Micrometrics TriStar II plus at 77

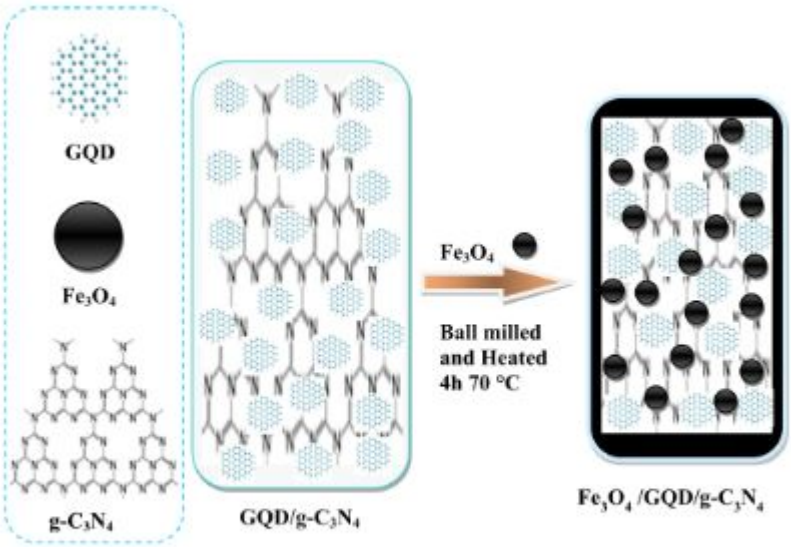

Fig. 1. Overall flowchart for the synthesis of (FGC) nanocomposite.

K. Before measurements, the sample was degassed at 100 °C for 12 h. The surface area was calculated according to BET equation and the pore size distribution was calculated using BJH approach from the adsorption branch of isotherm. UV-Vis diffuse reflectance spectroscopy (DRS) was recorded with an AvaSpec-2048 TEC spectrometer. Photoluminescence (PL) spectra of samples were recorded at room temperature using an Agilent-G980A instrument. The VSM profile was investigated by a (MDKB) vibrating sample magnetometer.

The photocatalytic performance was examined by RhB degradation at room temperature under visible light (150-W LED lamp) irradiation. In a typical experiment, 100 mg of photocatalysts were dispersed into 50 ml of 10 mg/L RhB aqueous solution, and then the mixed solution was stirred in the darkness for 30 min to get the adsorption-desorption equilibrium. During light irradiation, 5mL of the suspension was extracted, photocatalyst particles were separated using an external magnet and analysed to determine its residual concentration by a UV-vis spectrophotometer at the max absorbed wavelength of 562 nm. The degradation efficiency of the photocatalyst was calculated by the following equation:

$$\text{Degradation efficiency (\%)} = (C_0\text{-}C_t)\ /C_0 \times 100\ \% \quad (1)$$

Where C_0 and C_t represent the concentration of RhB at irradiation time zero and at reaction time
t, respectively.
The apparent first-order rate constant (k) can be obtained by fitting:

$$\ln (C_{t/}C_0) = -k_t \quad (2)$$

RESULTS AND DISCUSSION

The X-ray diffraction pattern (XRD) of the Fe_3O_4, g-C_3N_4 and FGC are presented in Fig. 2. The XRD spectrum of Fe_3O_4 exhibited diffraction peaks at 2θ = 17.76°, 30.04 °, 35.64 °, 43.4°, 57.32 °, and 63.24 °, which were well indexed to the (111) (220), (311), (400), (511), and (440) crystal planes of the spinel Fe_3O_4, respectively (JCPDS 96-900-5814) (Fig. 2a). The absence of other diffraction peaks indicates that the obtained nanoparticles were pure Fe_3O_4 with a spinel structure (Safee et al. 2010). Two peaks are observed in the g-C_3N_4 pattern, which indicates that melamine successfully transforms to g-C_3N_4. The strong peak at 27.4° corresponds to the (002) plane and is assigned to the interlayer stacking structure of the aromatic system, and the peak at 13.16° corresponds to the (100) plane and is attributed to the in-plane repeat unit of tri-s-triazine (JCPDS 96-047-1526) (Fig. 2b) (Wang et al. 2017). In the case of FGC, the XRD patterns are seen as the combination of patterns of g-C_3N_4 and Fe_3O_4 NPs. This diffraction pattern evidences the successful formation of ternary nanocomposite. However, the XRD peaks of GQD NPs are not clearly observed in the XRD patterns, which may be attributed to its low content. Also, the crystallite size of the synthesised material was found to be 6-10 nm by the Scherrer's formula, Dg = Kλ/βcosθ, where, D is the crystalline size, k (constant) = 0.9, λ (wavelength) = 1.54×10^{-10} m, β=full width half maximum (FWHM) and θ=diffraction angle.

The FTIR results of Fe_3O_4, g-C_3N_4 and FGC are shown in Fig. 3. In the spectrum of Fe_3O_4, peaks at ~600 and 1037 cm^{-1} were attributed to the Fe–O stretching vibration. The pronounced absorption at 1200–1600 cm^{-1} region is assigned to the stretching vibration of g-C_3N_4 heterocyclic, whereas the sharp peak at 809 cm^{-1} is observed as the typical breathing vibration of triazine units in the skeleton structure of g-C_3N_4. Moreover, in the case of the FGC, there was no significant change in the g-C_3N_4 spectrum after formation ternary composite, indicating that the FTIR spectrum is not sensitive enough to study the interaction between species, and there is no covalent band between the FGC components (Yang et al. 2010).

Surface morphology of Fe_3O_4, G/CN and FGC samples, was studied by FESEM technique

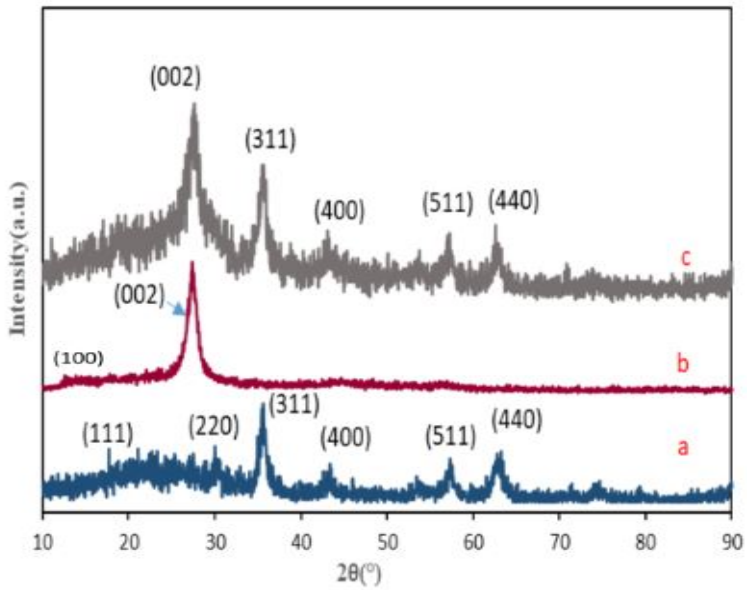

Fig. 2. XRD patterns of (a) Fe_3O_4, (b) g-C_3N_4 and (c) (FGC) nanocomposite.

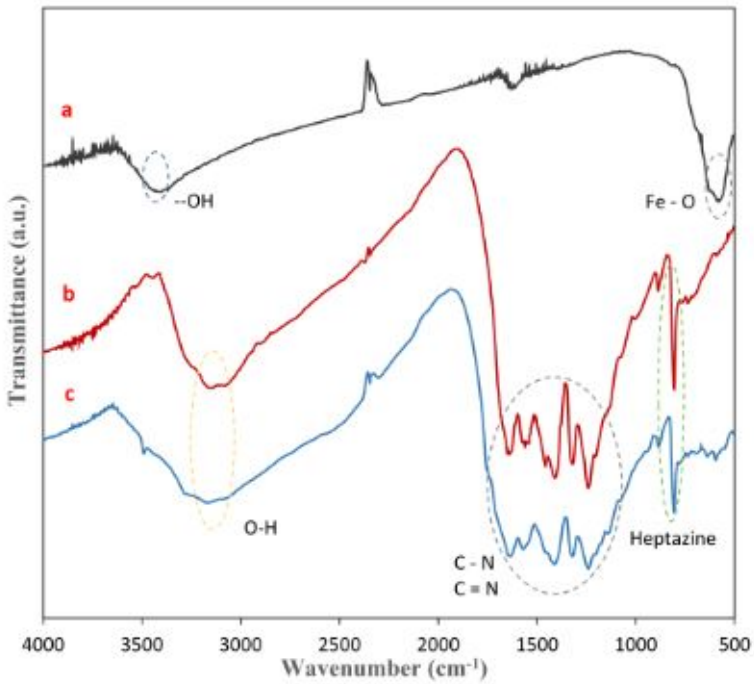

Fig. 3. FTIR spectra of (a) Fe_3O_4, (b) g-C_3N_4, (c) (FGC) nanocomposite.

(Fig. 4a-c). As observed, particles of Fe_3O_4 have accumulated on the surface of g-C_3N_4. The phase purity of FGC is studied by EDX, as well as elemental mapping and the corresponding results are shown in Fig. 5a and Table 1. Which reveal that the FGC consist of element Fe, O, C and N. The EDX elemental mapping graphs obviously demonstrated that the elements were uniformly distributed in the FCC. These results further validate the hybridization of pristine g-C_3N_4, GQD and Fe_3O_4 (Fig. 5b-f) (Wang et al. 2017; Rehman et al. 2019).

Efficiency of the photocatalysts in the separation of photogenerated electron-hole pairs is investigated with the help of PL spectroscopy. Intensity of a PL spectrum is directly proportional

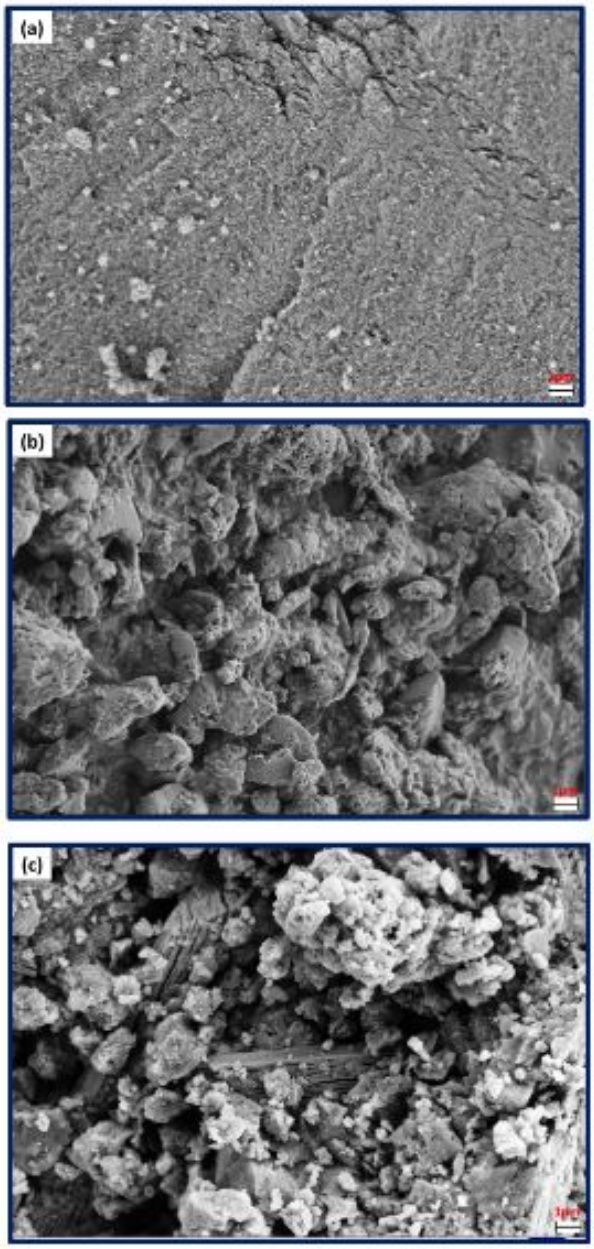

Fig. 4. FESEM images of (a) Fe_3O_4, (b) g-C_3N_4/GQD and (c) (FGC) nanocomposite.

to the recombination rate of the charge carriers. PL spectra, for GQD in Fig. 6, showed an intense peak at 460 nm owing to the recombination of fast photogenerated electrons and holes (Mitchell et al. 2014; Bayat & Saievar-Iranizad 2017). PL intensity decreased for G/CN after composite formation between GQD and g-C_3N_4. Moreover, the FGC displayed lower intensity compare to the pure GQD and G/CN, indicating that in the FGC the recombination of photogenerated electrons and holes was decreased.

Table 2 illustrates the textural properties of g-C_3N_4 and FGC photocatalyst, which was obtained by N_2 adsorbtion-desorbtion analysis. After the formation of FGC, compared to pure g-C_3N_4, specific surface area and pore volume has increased. The specific surface area of 14.2 and 22.9 m^2g^{-1} were calculated for g-C_3N_4 and FGC respectively. Therefore, active sites where are active centers of photocatalyst has raised, thus resulting in improvement of the photocatalytic performance (Zhou et al. 2013).

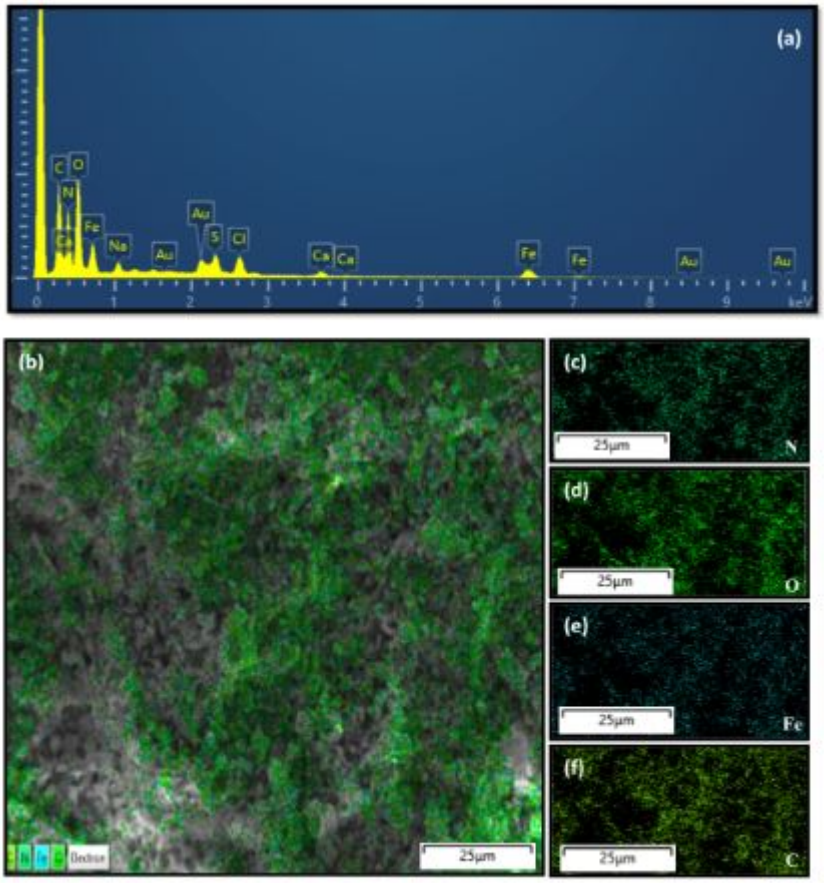

Fig. 5. (a) EDX spectra of (FGC) and (b-f) Elemental mapping image of the (FGC) nanocomposite.

Table 1. Basic composition of the produced materials represented by EDX analysis.

Samples	**Element (%)**			
	Fe	O	C	N
Fe_3O_4	38.54	61.46	-	-
GQD/ g-C_3N_4	-	5.18	47.65	47.17
FGC	9.59	22.37	34.38	33.63

Magnetic properties of the Fe_3O_4 NPs and FGC are shown in Fig.7. The saturation magnetization (Ms) of the Fe_3O_4 NPs was determined to be 61.70 emu/g. The FGC shows a maximum saturation magnetization of 12.09 emu/g, which is lower than pure Fe_3O_4 NPs due to the presence of nonmagnetic g-C_3N_4 and GQD NPs along with magnetic Fe_3O_4 NPs. Obviously, there is no any hysteresis, remanence, and coercivity in the magnetic hysteresis loops. Therefore, the samples are superparamagnetic and saturation magnetization of the nanocomposite is enough to separate particles from the solution using an external magnetic field (Zhu et al. 2008).

The photocatalytic activity of F/CN, G/CN and FGC photocatalysts was examined via degrading RhB in the presence of visible light. For the control experiments, before introducing the light irradiation, it achieves an adsorption-desorption equilibrium in the dark condition for 30 minutes. It can be observed from blank test that RhB is hardly degraded under visible and photocatalyst-free conditions, which proves that RhB is very stable in the aqueous solution. The FGC shows low photo-degradation efficiency of F/CN and G/CN within 70 min illumination.

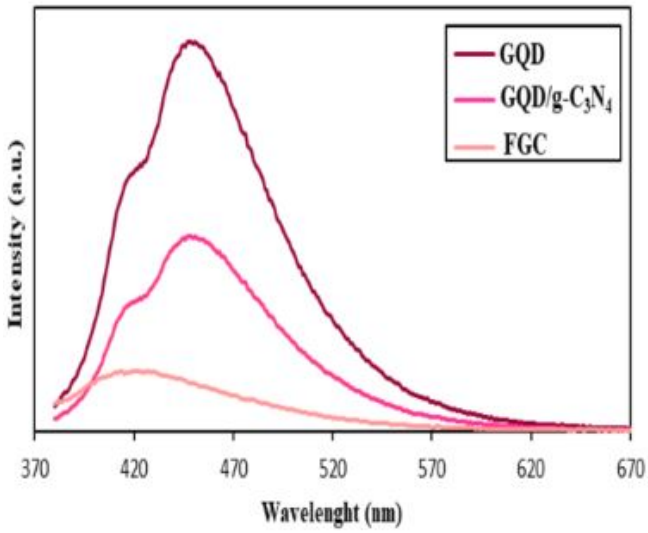

Fig. 6. PL spectra of GQD, GQD/ g-C_3N_4 and (FGC) nanocomposite.

Table 2. The details of samples, BET surface areas, BJH pore size, and the pore volumes of the as-synthesized samples.

Samples	BET surface area (m^2g^{-1})	Pore volume ($cm^3\ g^{-1}$)	Pore size (nm)
g-C_3N_4	14.2	0.048	14.24
FGC	22.9	0.099	22.39

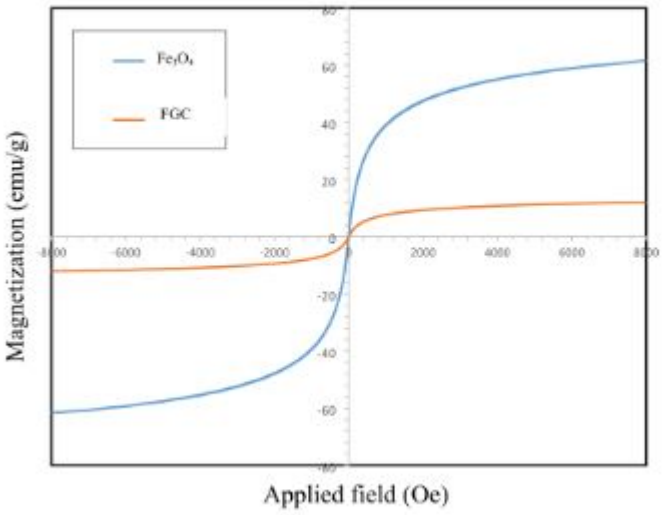

Fig. 7. VSM of Fe_3O_4 and FGC nanocomposite.

Interestingly, the photocatalytic activity of FGC was significantly increased after the addition of GQD and Fe_3O_4 to couple with the g-C_3N_4. FGC exhibited best degradation efficiency (100 %) as against that of other photocatalysts after 70 min illumination. This result is possibly attributed to the electrons transfer efficiency or the significantly improved visible light harvesting for ternary composite (Fig. 8a-b). As shown in Fig. 8c, the degradation data of RhB could be fitted by pseudo-first-order kinetic model. The apparent degradation constants of F/CN, G/CN and FGC samples are estimated to be 28.2×10^{-3}, 22×10^{-3} and 99×10^{-3} min^{-1}, respectively. Specifically, FGC

displays the highest rate constant for RhB degradation, nearly 3.5 and 4.5 times higher than F/CN and G/CN photocatalysts, respectively. These results indicate that FGC can effectively improve the photocatalytic efficiency of F/CN and G/CN. The enhanced photocatalytic performance can be attributed to the formation of heterogeneous, generating improved electron-hole separation and enhanced visible light absorption. Finally, the reusability of the FGC was examined by a cycle experiment of photocatalytic degradation of RhB. As shown in Fig. 8d, after four recycles, the prepared photocatalyst still show satisfied photocatalytic performance for the degradation of RhB, implying that the ternary photocatalyst is quite stable in the photocatalytic reaction.

Based on the above experimental results and the discussion, a practical mechanism for

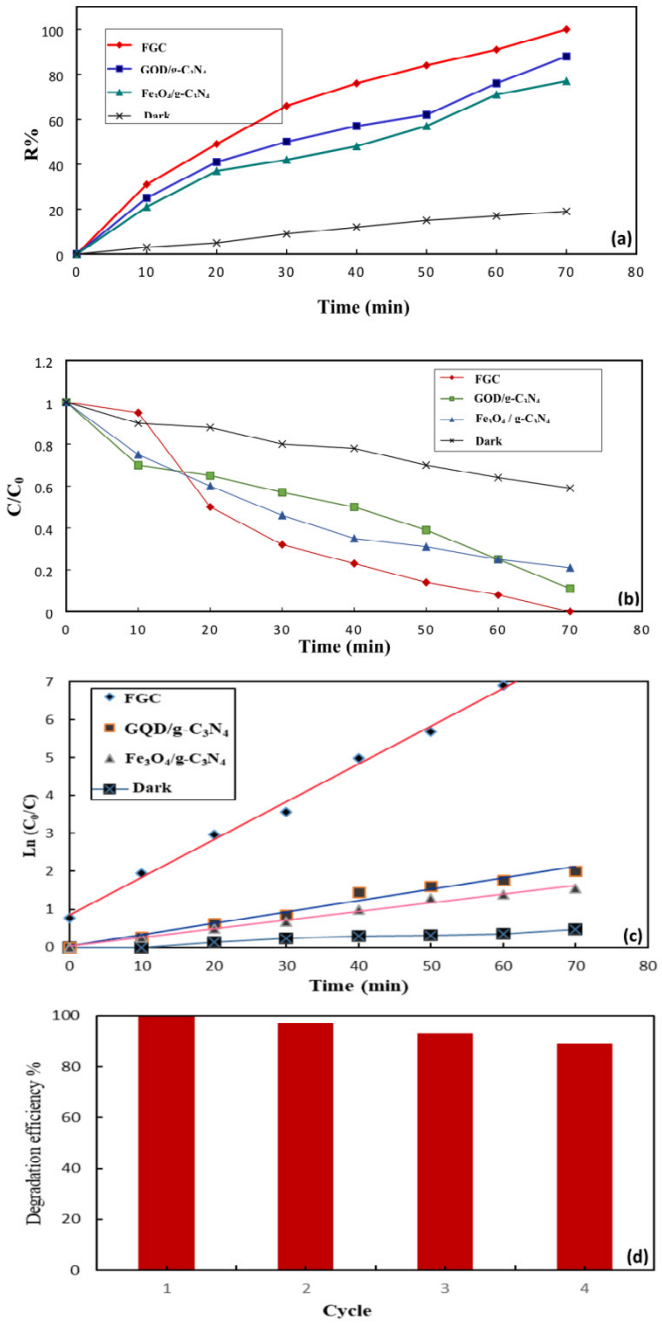

Fig. 8. (a) RhB removal efficiency during the photocatalytic experiments (b) Photodegradation curve for degradation of RhB over the fabricated samples (c) Pseudo-first order kinetic model of RhB photocatalysis (d) Cycle times on the photocatalytic activity of (FGC) nanocomposite.

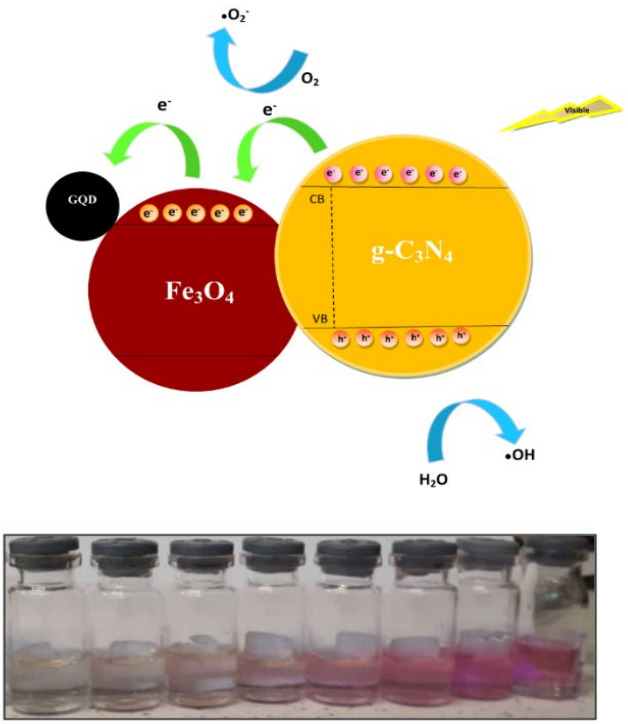

Fig. 9. proposed photocatalytic mechanism for degradation of RhB by (FGC) nanocomposite under visible light irradiation and degradation of RhB by (FGC) nanocomposite after 70 min.

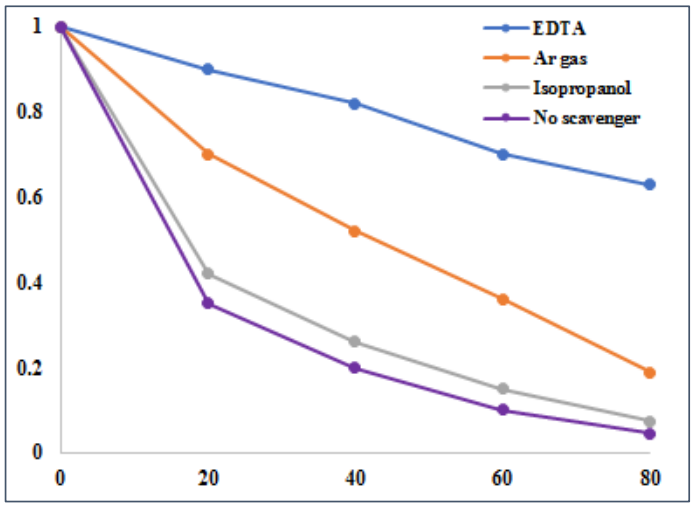

Fig. 10. Effects of a series of scavengers on the RhB photodegradation over FGC

degradation of RhB by FGC under the visible light irradiation is presented in Fig 9. The Schematic illustration shows the electron–hole separation processes and photodegradation mechanism of RhB. Firstly, when FGC is exposed to visible-light, the g-C_3N_4 produced electrons and holes. The electrons on conduction band of the g-C_3N_4 rapidly transfer to Fe_3O_4, and further transfer to GQD because of the good electrical conductivity of Fe_3O_4 and the electron storing capacity of GQD. Therefore, a part of photoelectrons on g-C_3N_4 conduction band by Fe_3O_4 transfer indirectly to GQD served as terminal electron acceptor, thus prolonging the photogenerated electrons lifetime and facilitating the charge carrier separation in the whole photocatalytic

system. This result has been confirmed by the PL spectra test. To further understand this process, we conducted experiments to identify the reactive species involved with the photodegradation of RhB. EDTA, argon gas, and isopropanol were selected to act as hole (h^+), superoxide radical ($^\bullet O_2^-$), and hydroxyl radical ($^\bullet OH$) scavengers, respectively. As shown in Fig. 10, the addition of isopropanol had no significant effects on the photodegradation of RhB by FGC, and thus $^\bullet OH$ was not involved in the process. By contrast, the addition of EDTA considerably reduced the degradation of RhB by the photocatalyst, which shows that h^+ played a major role. In addition, argon gas decreased the photocatalytic degradation of RhB to some extent, thereby indicating that $^\bullet O_2^-$ affected the photodegradation system, but its effect was less than that of h^+. In fact, the photo-induced electrons could reduce O_2 to $^\bullet O_2^-$, which affected the degradation of RhB. To further understand this process, we conducted experiments to identify the reactive species involved with the photodegradation of RhB. EDTA, argon gas, and isopropanol were selected to act as hole (h^+), superoxide radical ($^\bullet O_2^-$), and hydroxyl radical ($^\bullet OH$) scavengers, respectively. As shown in Fig. 10, the addition of isopropanol had no significant effects on the photodegradation of RhB by FGC, and thus $^\bullet OH$ was not involved in the process. By contrast, the addition of EDTA considerably reduced the degradation of RhB by the photocatalyst, which shows that h^+ played a major role. In addition, argon gas decreased the photocatalytic degradation of RhB to some extent, thereby indicating that $^\bullet O_2^-$ affected the photodegradation system, but its effect was less than that of h^+. In fact, the photo-induced electrons could reduce O_2 to $^\bullet O_2^-$, which affected the degradation of RhB (Ma et al. 2005; Liu et al. 2014). Furthermore, Photographs of RhB solution before and after the addition of FGC were shown in Fig. 9.

CONCLUSIONS

Briefly, we successfully prepared ternary magnetic FGC nanocomposite, as highly enhanced visible-light-active photocatalyst. Photocatalytic activity of the photocatalysts was evaluated by degradation of RhB under the visible-light irradiation. Among the prepared samples, ternary composite has the best activity. The photocatalytic activity of FGC nanocomposite is higher than those of the F/CN and G/CN nanocomposites in degradation of RhB under the visible-light irradiation. The enhanced activity of the FGC nanocomposite was assigned to more harvesting of the visible-light illumination and more efficiently separation of the photogenerated charge carriers. The as-prepared photocatalyst can be washed and reused several times because of the strong magnetism. The photodegradation kinetics and possible reaction mechanism were also evaluated.

ACKNOWLEDGMENT

The Authors wish to acknowledge University of Semnan and University of Tehran, for financial support of this work.

GRANT SUPPORT DETAILS

The present research did not receive any financial support.

CONFLICT OF INTEREST

The authors declare that there is not any conflict of interests regarding the publication of this manuscript. In addition, the ethical issues, including plagiarism, informed consent, misconduct, data fabrication and/ or falsification, double publication and/or submission, and redundancy has been completely observed by the authors.

LIFE SCIENCE REPORTING

No life science threat was practiced in this research.

REFERENCES

Akhundi, A., Badiei, A. and Ziarani, G. M. (2020). Graphitic carbon nitride-based photocatalysts: toward efficient organic transformation for value-added chemicals production. Mol. Catal. 488; 110902-110912.

Akhundi, A. and Habibi-Yangjeh, A. (2016). Facile preparation of novel quaternary g-C_3N_4/Fe_3O_4/AgI/Bi_2S_3 nanocomposites: magnetically separable visible-light-driven photocatalysts with significantly enhanced activity. RSC Adv., 6(108); 106572–106583.

Alsaleh, M. and Abdul-Rahim, A. S. (2021). The nexus between worldwide governance indicators and hydropower sustainable growth in EU 28 region. Int. J. Environ. Res., 15(6); 1–15.

Azimi, EB., Badiei, A. and Sadr, M. H. (2018a). Dramatic visible photocatalytic performance of g-C_3N_4-based nanocomposite due to the synergistic effect of AgBr and ZnO semiconductors. J. Phys. Chem. Solids, 122; 174–183.

Azimi, E. B., Badiei, A., Sadr, MH. and Amiri, A. (2018b). A template-free method to synthesize porous g-C_3N_4 with efficient visible light photodegradation of organic pollutants in water. Adv. Powder Technol., 29(11); 2785–2791.

Barvin, R. K. B., Prakash, P., Ganesh, V. and Jeyaprabha, B. (2019). Highly selective and sensitive sensing of toxic mercury ions utilizing carbon quantum dot-modified glassy carbon electrode, Int. J. Environ. Res., 13(6); 1015–1023.

Bayat, A. and Saievar-Iranizad, E. (2017). Synthesis of green-photoluminescent single layer graphene quantum dots: determination of HOMO and LUMO energy states' J. Lumin., 192; 180–183.

Dai, K., Lu, L., Liu, Q., Zhu, G., Wei, X., Bai, J., Xuan, L. and Wang, H. (2014). Sonication assisted preparation of graphene oxide/graphitic-C3N4 nanosheet hybrid with reinforced photocurrent for photocatalyst applications, Dalt. Trans., 43(17); 6295–6299.

Dalrymple, O. K., Stefanakos, E., Trotz, M. A. and Goswami, DY. (2010). A review of the mechanisms and modeling of photocatalytic disinfection, Appl. Catal. B Environ., 98(1-2); 27–38.

Esplugas, S., Gimenez, J., Contreras, S., Pascual, E. and Rodrıguez, M. (2002). Comparison of different advanced oxidation processes for phenol degradation. Water. Res., 36(4); 1034–1042.

Ghanbari, M. and Salavati-Niasari, M. (2018). Tl_4CdI_6 nanostructures: facile sonochemical synthesis and photocatalytic activity for removal of organic dyes' Inorg. Chem., 57(18); 11443–11455.

Giannakis, S. Rtimi, S. and Pulgarin, C. (2017). Light-assisted advanced oxidation processes for the elimination of chemical and microbiological pollution of wastewaters in developed and developing countries. Molecules, 22(7); 1070.

Hong, Y., Meng, Y., Zhang, G., Yin, B., Zhao, Y., Shi, W. and Li, C. (2016). Facile fabrication of stable metal-free CQDs/g-C_3N_4 heterojunctions with efficiently enhanced visible-light photocatalytic activity. Sep. Purif. Technol., 171; 229–237.

Karami, M., Ghanbari, Amiri, O. and Salavati-Niasari, M. (2020). Enhanced antibacterial activity and photocatalytic degradation of organic dyes under visible light using cesium lead iodide perovskite nanostructures prepared by hydrothermal method. Sep. Purif. Technol., 253; 117526.

Liu, C. G., Wu, X. T., Li, X. F. and Zhang, XG. (2014). Synthesis of graphene-like g-C_3N_4/Fe_3O_4 nanocomposites with high photocatalytic activity and applications in drug delivery. RSC Adv., 4(107); 62492–62498.

Ma, Z., Guan, Y. and Liu, H. (2005). Synthesis and characterization of micron-sized monodisperse superparamagnetic polymer particles with amino groups. J. Polym. Sci. Part. A Polym. Chem., 43(15); 3433–3439.

Mitchell, B., Siobhan, J. B. and Thomas, N. (2014). Graphene quantum dots. Part. Part. Syst. Char., 31(4); 415–428.

Mousavi, M. and Habibi-Yangjeh, A. (2017). Novel magnetically separable g-C_3N_4/Fe_3O_4/Ag_3PO_4/Co_3O_4 nanocomposites: visible-light-driven photocatalysts with highly enhanced activity,. Adv. Powder Technol., 28(6); 1540–1553.

Naik, J. P., Sutradhar, P. and Saha, M. (2017). Molecular scale rapid synthesis of graphene quantum dots

(GQDs), J. Nanostructure Chem., 7(1); 85–89.
Palmisano, G., Augugliaro, V., Pagliaro, M. and Palmisano, L. (2007). Photocatalysis: a promising route for 21st century organic chemistry. Chem. Commun., 33; 3425–3437.
Rehman, G. U., Tahir, M., Goh, P. S., Ismail, A. F., Samavati, A. and Zulhairun, A. K. (2019). Facile synthesis of GO and g-C3N4 nanosheets encapsulated magnetite ternary nanocomposite for superior photocatalytic degradation of phenol. Environ. Pollut., 253; 1066–1078.
Safee, N. H. A., Abdullah, M. P. and Othman, M.R. (2010). Carboxymethyl chitosan-Fe_3O_4 nanoparticles: synthesis and characterization. Malays. J. Anal. Sci., 14(2); 63–68.
Sudhaik, A. Raizada, P., Shandilya, P., Jeong, D. Y., Lim, J. H. and Singh, P. (2018). Review on fabrication of graphitic carbon nitride based efficient nanocomposites for photodegradation of aqueous phase organic pollutants. J. Ind. Eng. Chem., 67; 28–51.
Tong, Z., Yang, D., Shi, J., Nan, Y., Sun, Y. and Jiang, Z. (2015). Three-dimensional porous aerogel constructed by g-C_3N_4 and graphene oxide nanosheets with excellent visible-light photocatalytic performance. ACS Appl. Mater. Interfaces, 7(46); 25693–25701.
Wang, R., Xie, T., Sun, Z., Pu, T., Li, W. and Ao, J. P. (2017). Graphene quantum dot modified g-C3N4 for enhanced photocatalytic oxidation of ammonia performance. RSC Adv., 7(81); 51687–51694.
Yahya, N., Aziz, F., Jamaludin, N. A., Mutalib, M. A., Ismail, A. F., Salleh, W. N. W., Jaafar, J., Yusof, N. and Ludin, N. A. (2018). A review of integrated photocatalyst adsorbents for wastewater treatment. J. Environ. Chem. Eng., 6(6); 7411–7425.
Yang, K., Peng, H., Wen, Y. and Li, N. (2010). Re-examination of characteristic FTIR spectrum of secondary layer in bilayer oleic acid-coated Fe_3O_4 nanoparticles. Appl. Surf. Sci., 256(10); 3093–3097.
Zhang, N., Zhang, Y. and Xu. Y. J. (2012). Recent progress on graphene-based photocatalysts: current status and future perspectives. Nanoscale, 4(19); 5792–5813.
Zheng, Y., Liu, J., Liang, J., Jaroniec, M. and Qiao, S.Z. (2012). Graphitic carbon nitride materials: controllable synthesis and applications in fuel cells and photocatalysis. Energy Environ. Sci., 5(5); 6717–6731.
Zhou, X., Jin, B., Chen, R., Peng, F. and Fang, Y. (2013). Synthesis of porous Fe_3O_4/g-C_3N_4 nanospheres as highly efficient and recyclable photocatalysts. Mater. Res. Bull., 48(4); 1447–1452.
Zhu, A., Yuan, L, and Liao, T. (2008). Suspension of Fe_3O_4 nanoparticles stabilized by chitosan and o-carboxymethylchitosan. Int. J. Pharm., 350(1-2); 361–368.